JGR Space Physics

RESEARCH ARTICLE
10.1029/2024JA033155

Key Points:

- To project low-altitude ELFIN measurements of energetic electron fluxes we perform a statistical comparison of ELFIN and GPS measurements
- We develop a model for the phase space mapping of low-altitude ELFIN measurements onto equatorial plane
- We validate our model using Arase/ERG measurements of energetic electron fluxes

Supporting Information:

Supporting Information may be found in the online version of this article.

Correspondence to:

W. Sun,
weiqin.sun@utdallas.edu

Citation:

Sun, W., Zhang, X.-J., Artemyev, A. V., Mourenas, D., Morley, S. K., Angelopoulos, V., et al. (2024). ELFIN-GPS comparison of energetic electron fluxes: Modeling low-altitude electron flux mapping to the equatorial magnetosphere. *Journal of Geophysical Research: Space Physics*, *129*, e2024JA033155. https://doi.org/10.1029/2024JA033155

Received 7 AUG 2024
Accepted 18 OCT 2024

Author Contributions:

Conceptualization: Xiao-Jia Zhang, Anton V. Artemyev
Data curation: Xiao-Jia Zhang, Anton V. Artemyev, Steven K. Morley, Vassilis Angelopoulos, S. Kasahara, Y. Miyoshi, A. Matsuoka, T. Mitani, S. Yokota, T. Hori, K. Keika, T. Takashima, M. Teramoto, I. Shinohara, K. Yamamoto
Funding acquisition: Xiao-Jia Zhang, Anton V. Artemyev
Methodology: Xiao-Jia Zhang, Anton V. Artemyev
Project administration: Xiao-Jia Zhang, Anton V. Artemyev
Resources: Xiao-Jia Zhang, Anton V. Artemyev, Steven K. Morley
Supervision: Xiao-Jia Zhang, Anton V. Artemyev

ELFIN-GPS Comparison of Energetic Electron Fluxes: Modeling Low-Altitude Electron Flux Mapping to the Equatorial Magnetosphere

Weiqin Sun[1], Xiao-Jia Zhang[1,2], Anton V. Artemyev[2], Didier Mourenas[3,4], Steven K. Morley[5], Vassilis Angelopoulos[2], S. Kasahara[6], Y. Miyoshi[7], A. Matsuoka[8], T. Mitani[9], S. Yokota[10], T. Hori[7], K. Keika[6], T. Takashima[9], M. Teramoto[10], I. Shinohara[9], and K. Yamamoto[7]

[1]Department of Physics, University of Texas at Dallas, Richardson, TX, USA, [2]Department of Earth, Planetary, and Space Sciences, University of California, Los Angeles, CA, USA, [3]CEA, DAM, DIF, Arpajon, France, [4]Laboratoire Matière en Conditions Extrêmes, Université Paris-Saclay, CEA, Orsay, France, [5]Space Science and Applications, Los Alamos National Laboratory, Los Alamos, NM, USA, [6]Department of Earth and Planetary Science, School of Science, The University of Tokyo, Tokyo, Japan, [7]Institute for Space Earth Environmental Research, Nagoya University, Nagoya, Japan, [8]Graduate School of Science, Kyoto University, Kyoto, Japan, [9]Institute of Space and Astronautical Science, Japan Aerospace Exploration Agency, Sagamihara, Japan, [10]Faculty of Engineering, Department of Space Systems Engineering, Kyushu Institute of Technology, Kitakyushu, Japan

Abstract Near-equatorial measurements of energetic electron fluxes, in combination with numerical simulation, are widely used for monitoring of the radiation belt dynamics. However, the long orbital periods of near-equatorial spacecraft constrain the cadence of observations to once per several hours or greater, that is, much longer than the mesoscale injections and rapid local acceleration and losses of energetic electrons of interest. An alternative approach for radiation belt monitoring is to use measurements of low-altitude spacecraft, which cover, once per hour or faster, the latitudinal range of the entire radiation belt within a few minutes. Such an approach requires, however, a procedure for mapping the flux from low equatorial pitch angles (near the loss cone) as measured at low altitude, to high equatorial pitch angles (far from the loss cone), as necessitated by equatorial flux models. Here we do this using the high energy resolution ELFIN measurements of energetic electrons. Combining those with GPS measurements we develop a model for the electron anisotropy coefficient, n, that describes electron flux j_{trap} dependence on equatorial pitch-angle, α_{eq}, $j_{trap} \sim \sin^n \alpha_{eq}$. We then validate this model by comparing its equatorial predictions from ELFIN with in-situ near-equatorial measurements from Arase (ERG) in the outer radiation belt.

1. Introduction

The dynamics of Earth's outer radiation belt, an important element of space weather (Horne et al., 2013), entails various processes operating on a wide range of spatial and temporal scales. The variability of energetic electron fluxes on a time scale of geomagnetic storms, taking hours to days, is well captured by near-equatorial spacecraft measurements probing flux dynamics with cadence of a few hours, based on their orbital period (see examples in Allison et al., 2021; Li et al., 2014; Ma et al., 2018; Tu et al., 2014; Turner, O'Brien et al., 2015; Thorne et al., 2013). Shorter time scales (below a couple of hours) and spatially localized substorm dynamics are much less well resolved by equatorial missions that, at best, can detect the substorm injection (e.g., Gabrielse et al., 2014, 2019; Turner, Claudepierre, et al., 2015), but cannot follow electron flux dynamics on sub-orbital times (see discussion in Turner et al., 2017). Therefore, the growing interest in such substorm-scale (or meso-scale) dynamics of the radiation belt has driven the development of new observational techniques. Besides the approach proposed by Morley, Friedel, Cayton, and Noveroske (2010) with utilization of tens of GPS spacecraft (see details in Morley et al., 2016; Boynton et al., 2017; Smirnov et al., 2020; Olifer et al., 2024) equipped by Combined X-ray Dosimeter measuring energetic electron fluxes (see Morley et al., 2017; Morley, Friedel, Spanswick, et al., 2010), the most promising method for tracing temporally and spatially localized electron flux dynamics is based on analysis of low-altitude spacecraft measurements (Allison et al., 2018; Botek et al., 2023; Claudepierre & O'Brien, 2020; Ginisty et al., 2023; Winant et al., 2023). Such spacecraft cross the low-altitude projection of the entire inner magnetosphere within several minutes and may provide snapshot-like vision of spatially resolved electron flux dynamics. The main challenge for this method consists in the reconstruction of

Writing – review & editing: Xiao-Jia Zhang, Anton V. Artemyev, Didier Mourenas, Steven K. Morley, Vassilis Angelopoulos, S. Kasahara, Y. Miyoshi, A. Matsuoka, T. Mitani, S. Yokota, T. Hori, K. Keika, T. Takashima, M. Teramoto, I. Shinohara, K. Yamamoto

equatorial fluxes from measurements of a small fraction of the electron distribution (only small pitch-angles) at low altitudes (see discussion in Boyd et al., 2023; Drozdov et al., 2023).

Existing models for tracing the radiation belt dynamics with low-altitude measurements utilize the dataset provided by the fleet of Polar Operational Environmental Satellites (POES/NOAA) and MetOp satellites (Evans & Greer, 2004), which have a poor energy resolution (see examples of such models in Allison et al., 2018; Claudepierre & O'Brien, 2020; Boyd et al., 2023; Drozdov et al., 2023). In this study we would like to take advantage of a new, recently available, dataset of high energy resolution measurements of electron fluxes by a couple low-altitude Electron Losses and Fields Investigation (ELFIN) CubeSats (Angelopoulos et al., 2020). Although the ELFIN dataset does not provide a comparable temporal coverage as the multiple POES satellites, ELFIN covered well the main magnetospheric storm intervals during the 2020–2022 period (see details in Tsai et al., 2024). Moreover, having 16 energy channels from 50 keV to 6 MeV ELFIN traces well the different drivers of energetic electron flux dynamics, including slow electron flux decay due to scattering by hiss waves (Mourenas et al., 2021), rapid transient flux variations due to substorm injections (Artemyev et al., 2024) and precipitations by electromagnetic ion cyclotron waves (Angelopoulos et al., 2023; Capannolo et al., 2023), and other meso-scale magnetospheric processes (see discussion in Zhang et al., 2023).

To construct a model for the phase space mapping of low-altitude ELFIN measurements onto the equatorial plane, we compare (energy, L-shell) flux distributions collected by ELFIN and by the fleet of GPS satellites (Morley et al., 2016; Morley, Friedel, Spanswick, et al., 2010). The main advance of this approach consists in utilizing a sufficient number of GPS satellites to obtain (energy, L-shell) flux distributions within a couple of hours from ELFIN measurements. Using near-equatorial spacecraft would require a much longer interval to collect the full (energy, L-shell) flux distribution for the L-shell range of the outer radiation belt, which would not yield a sufficient number of conjugate observations with ELFIN. Comparison of GPS and ELFIN energy, L-shell flux distributions, we derive the anisotropy coefficient $n = n(E,L,AE)$, such that the equatorial electron flux is described as $j(E,\alpha) = j_0(E)\sin^n(\alpha)$ (Chen et al., 2014; Gannon et al., 2007; Shi et al., 2016; Zhao et al., 2018). This coefficient allows the phase space mapping of ELFIN measurements $j_{ELFIN}(E)$ to the equator: $j_0(E) = j_{ELFIN}(E)\cdot(B_{ELFIN}/B_0)^{n/2}$ for given geomagnetic activity parameterized by AE index and L-shell (B_{ELFIN} and B_0 are magnetic fields at the ELFIN altitude and at the equator). To verify the derived model of $n = n(E,L,AE)$ we next compare the phase space mapping of ELFIN fluxes with measurements of Exploration of energization and Radiation in Geospace (Arase, ERG) satellite (Miyoshi, Hori, et al., 2018).

The paper consists of five Sections: in Section 2 we describe the main ELFIN, GPS, and Arase datasets and instruments of energetic particle measurements, in Section 3 we show ELFIN/GPS comparison and construction of n model, in Section 4 we verify our model through several comparisons of ELFIN and Arase measurements, and in Section 5 we discuss and summarize the obtained results.

2. Data Set

The main dataset consists of energetic electron measurements by ELFIN CubeSats, at ∼440 km altitude (Angelopoulos et al., 2020). ELFIN energetic electron detector measures electrons between 50 keV and 6 MeV energy with an energy resolution $\Delta E/E \leq 40\%$. The entire 180° range of pitch-angles can be covered twice every 3 s, the ELFIN spin period. We use two data products of ELFIN: spectra of locally trapped electron fluxes, j_{perp} (pitch-angle averaged outside of the local loss cone) and precipitating fluxes, j_{loss} (pitch-angle averaged inside the loss cone) (see details Angelopoulos et al., 2023). We use energetic electron measurements by GPS spacecraft (#53–61, excluding #54): 4 minute resolution of Combined X-ray Dosimeter (CXD) (Carver et al., 2020; Morley et al., 2017) at 15 evaluated energies (from 120 to 10,000 keV), as provided in the v1.10 GPS energetic particle data product archived by NOAA (see Open Research section for details). These energies lie within the range of CXD's Low Energy Particle (LEP) sensor (Tuszewski et al., 2004) and are obtained by flux forward modeling and cross-calibrated with Van Allen Probes (Mauk et al., 2013) measurements as described by Morley et al. (2016).

To verify the proposed model of anisotropy coefficient, we also use energetic electron measurements provided by the Medium-energy particle experiments - electron analyzer (MEPe) (Kasahara, Yokota, Hori, et al., 2018) with 8 s resolution at 15 energies (from 7.0 to 87.5 keV) and the High-energy electron experiments (HEP) (Mitani, Takashima, et al., 2018) with 8 s resolution at 16 energies (from 60.2 to 1,590.8 keV) onboard Arase/ERG (Miyoshi, Shinohara, & Jun, 2018). For comparison of low-altitude ELFIN measurements and near-equatorial

GPS, Arase measurements, we project ELFIN orbit to equator using the IGRF field. For GPS and Arase measurements, we use both the IGRF field and the T89 (Tsyganenko, 1989) magnetic field model. Using more sophisticated than IGRF magnetic field models for the phase space mapping of ELFIN results in significant uncertainties in the night-side region (see discussion in Artemyev et al., 2022), but to account for the difference between IGRF and the T89 (Tsyganenko, 1989) magnetic field models, we use the linear shift of ELFIN L-shells to match the peak relativistic fluxes with Arase or GPS flux distribution.

3. ELFIN/GPS Model

We start with a brief description of typical events used to compare GPS and ELFIN fluxes and determine the anisotropy coefficient n. Figure 1 provides an overview of three such events with combined ELFIN/GPS measurements under different geomagnetic conditions parametrized by SME indices ($0 < \text{SME} \leq 100$ nT, 100 nT $<$ SME $\leq$ 300 nT and SME $>$ 300 nT). Figures 1a–1f illustrate the main types of data products for the event with $0 < \text{SME} \leq 100$ nT, where the maxima of the one-hour SME index preceding the ELFIN measurements falls within the range of 0–100. In Figure 1a, the one-hour SuperMAG SME SMU and SML auroral electrojet indices (SuperMAG analogs of standard AE, AU, and AL indices, see Gjerloev, 2012) preceding the ELFIN measurements are displayed, with the ELFIN measurement interval highlighted by a pink dashed rectangle. Figures 1b and 1c present details of ELFIN measurements, showcasing the ratio of precipitating (within the bounce loss cone) to trapped (outside of the bounce loss cone) fluxes of electrons and the electron trapped flux during ELFIN orbit on 16 July 2020, at $L = 4 \sim 10$. There is no strong precipitation event during the quiet time interval of ELFIN measurements, with a precipitation-to-trapped ratio below 0.1 for the entire L-shell range.

In accordance with our criteria for selecting conjugate measurements, GPS spacecraft encompass trajectories that partially overlap within ±3 hours of MLT and ±2 hours of UT around ELFIN measurements (see Figure S1 in Supporting Information S1 for details regarding the selected GPS trajectories). We combine GPS electron flux from the eligible GPS orbits and average them to provide a L-shell, energy flux distribution with an L resolution of 0.25 (see also Figure S1 in Supporting Information S1 for the averaged GPS electron flux). The averaged GPS fluxes are then interpolated at the same energies as ELFIN, depicted in Figure 1d. It is worth noting that the lowest energy channel of GPS electron measurements is 120 keV. Therefore, extrapolating the GPS flux to the energy of 63 keV (a channel available on ELFIN) may not yield reasonable results.

Under the assumption that ELFIN observed the same electron population as GPS satellites, except for a possible L-shell shift due to uncertainties in the phase space mapping of ELFIN to the equator, we align the interpolated electron trapped flux of ELFIN measurements with the local maximum of the interpolated electron flux of GPS spacecraft, finally obtaining Figure 1e. We calculate the displacement for each ELFIN/GPS comparison event and then determine the average δL for three geomagnetic activity ranges: $\delta L = (-0.5, -0.5, -0.25)$ (with further details provided in the statistical sections). Consequently, the displacement of L for $0 < \text{SME} \leq 100$ nT is shown at the top of Figure 1e. These values can be further used to project ELFIN measurements to the equatorial plane using the anisotropy index model.

We suppose that the $\sin^n \alpha$ form can adequately represent the majority of the Pitch Angle Distributions (PADs). Although this may not be entirely accurate, it provides us with a preliminary approximation of PADs, necessary for the present statistical analysis. Thus, at the equatorial plane, the flux j_{eq} of electrons with a pitch angle (PA) α_{eq} can be expressed as $j_{eq}(\alpha_{eq}) = j_0 \sin^n \alpha_{eq}$, where j_0 represents the flux of electrons with a PA of 90° and can be expressed through the omnidirectional flux. Since flux is conserved along geomagnetic field lines (Roederer, 1970), the flux j_{GPS} at GPS altitude is given by $j_{GPS}(\alpha_{GPS}) = j_{eq}(\alpha_{eq})$ with α_{GPS} the local PA at GPS spacecraft corresponding to α_{eq} at the equator. Note here we assume the $\sin^n \alpha$ form for fluxes and use measured omnidirectional GPS flux to define $j_{GPS}(\alpha_{GPS}) = j_{eq}(\alpha_{eq})$. The conservation of the first adiabatic invariant implies that $\sin\alpha_{eq} = \sqrt{B_{eq}/B_{GPS}} \sin\alpha_{GPS}$, giving:

$$j_{GPS}(\alpha_{GPS}) = j_0 (B_{eq}/B_{GPS})^{n/2} \sin^n \alpha_{GPS} \quad (1)$$

In this study, we use omnidirectional fluxes measured by GPS spacecraft (see details in Olifer et al., 2024), which correspond to fluxes averaged over α, $\langle j_{GPS} \rangle$, given by:

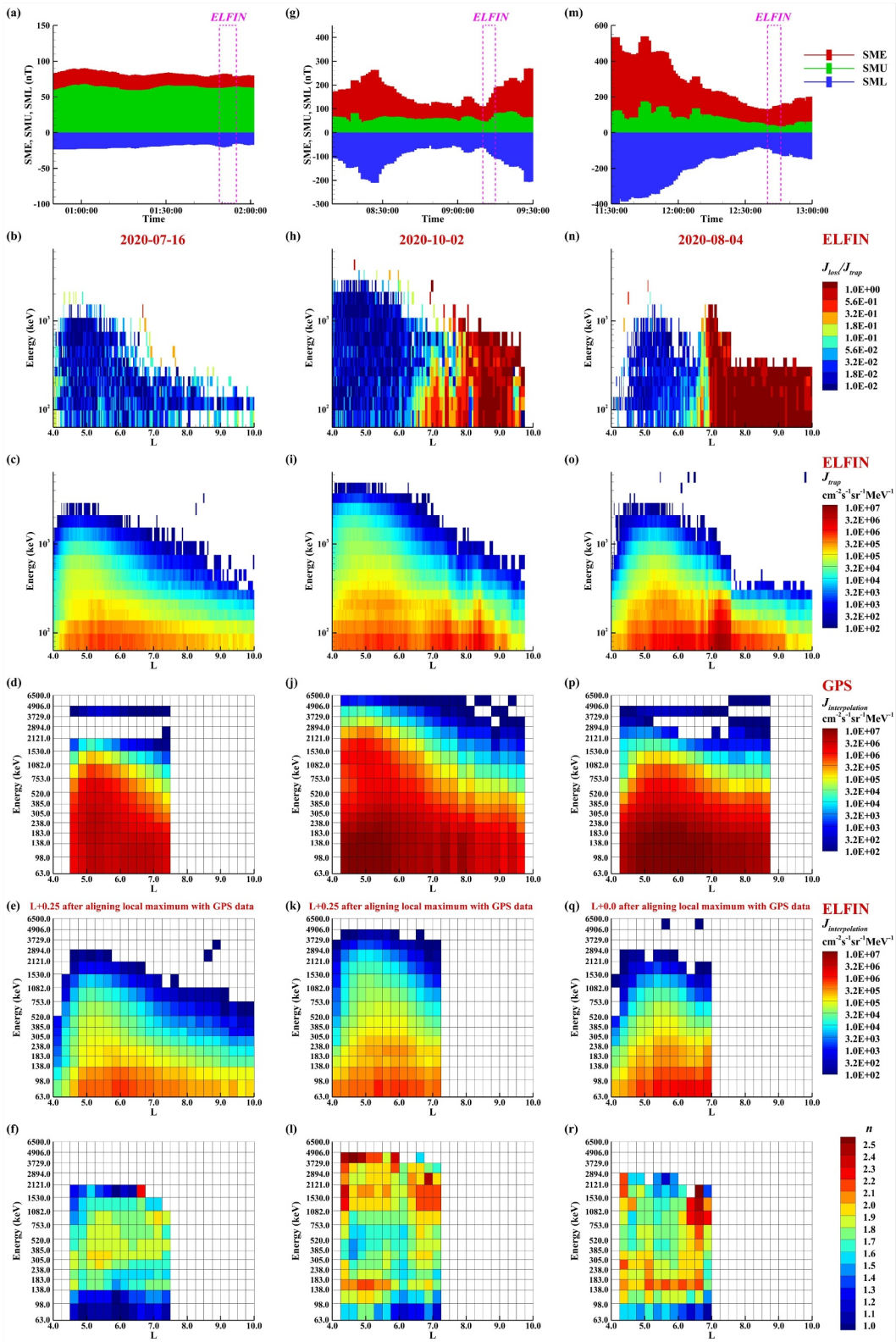

Figure 1.

$$\langle j_{GPS} \rangle = j_0 (B_{eq}/B_{GPS})^{n/2} \langle \sin^n \alpha_{GPS} \rangle = j_0 (B_{eq}/B_{GPS})^{n/2} C_n \quad (2)$$

Similarly for ELFIN, the ELFIN perpendicular flux (outside of the bounce loss cone) $j_{ELFIN\perp}$ can be written approximately as:

$$j_{ELFIN\perp} = j_0 (B_{eq}/B_{ELFIN})^{n/2}$$

Hence, we can establish the relationship:

$$\frac{j_{ELFIN\perp} C_n}{\langle j_{GPS} \rangle} = \left(\frac{B_{GPS}}{B_{ELFIN}} \right)^{n/2} \quad (3)$$

The anisotropy coefficient n can be expressed as:

$$n = \ln \frac{j_{ELFIN\perp} C_n}{\langle j_{GPS} \rangle} \Bigg/ \ln \left(\frac{B_{GPS}}{B_{ELFIN}} \right)^{1/2} \quad (4)$$

Therefore, utilizing Figures 1d and 1e alongside the magnetic field magnitudes at ELFIN and GPS altitudes, we calculate the anisotropy coefficient n using Equation 4, presented in Figure 1f. As mentioned above, the extrapolated GPS flux at 63 keV may not provide accurate results, possibly explaining the underestimation of n at 63 keV.

Figures 1g–1l and 1m–1r illustrate two additional ELFIN/GPS combined events belonging to the category of 100 nT < SME ≤ 300 nT and SME ≥ 300 nT, respectively, in the same format as Figures 1a–1f. Additional details regarding the selected GPS trajectories and averaged GPS electron flux are provided in Figures S2 and S3 in Supporting Information S1. Comparatively, Figures 1h and 1n highlight a significant penetration of the plasma sheet into lower L-shells during moderate and strongly disturbed conditions, in contrast to Figure 1b. Electron field line curvature scattering within the plasma sheet is well seen as a large precipitation-to-trapped flux ratio (reaching ∼1) at large L-shells (see Artemyev et al., 2022; Wilkins et al., 2023). We mask the region where the precipitating-to-trapped flux ratio exceeds 0.5 and do not use the corresponding ELFIN measurements. Note that although Figures 1f–1l and 1r show that the electron anisotropy parameter is larger during more disturbed geomagnetic conditions, this is not the typical case. Statistical results usually show a decrease in the anisotropy parameter with increasing geomagnetic activity, likely due to enhanced pitch-angle scattering by waves. The unusually low anisotropy parameter for the 2020-07-16 event can be explained by the fact that these few hours of geomagnetically quiet observations occurred during the recovery phase of a geomagnetic storm. During this phase, the pitch-angle distributions of equatorial electrons were likely well isotropized due to wave wave-particle interactions before ELFIN observations. There is also an interesting energy, L-shell distribution of n with larger values at higher energies, and lower n at intermediate energies. We checked this distribution during statistical ELFIN/GPS comparisons and provide some speculations about its possible origins in the Discussion section.

To acquire a statistical overview of the anisotropy coefficient n, we implemented the criteria for selecting GPS trajectories corresponding to ELFIN events spanning from March 2020 to February 2022. This process resulted in a database comprising 211 ELFIN/GPS combined events. Figure 2 presents an overview of the anisotropy coefficient n averaged over these 211 ELFIN/GPS combined events for different SME ranges (0 < SME ≤ 100 nT, 100 nT < SME ≤ 300 nT and SME > 300 nT). Figures 2a–2c illustrate the distribution of n at $L = 4 \sim 10$, averaged from 50, 85 and 76 cases respectively for different SME ranges (see Figure S4 in Supporting Information S1 for the average event number per grid point across different SME indices). The average and standard

Figure 1. Overview of three ELFIN/GPS combined events under different geomagnetic conditions parametrized by SME index (0 < SME ≤ 100 nT, 100 nT < SME ≤ 300 nT and SME > 300 nT) (a,g,m) One-hour SuperMAG SME SMU and SML auroral electrojet indices preceding the ELFIN measurements (indicated by the pink dashed rectangle) (b,h,n) The ratio of precipitating (within the bounce loss cone) to trapped (outside of the bounce loss cone) flux of electrons during ELFIN trajectories (c,i,o) Electron trapped flux of the same ELFIN trajectories (d,j,p) The interpolated electron flux of GPS measurements from trajectories that partially overlap within ±3 hr of MLT and ±2 hr of UT around ELFIN measurements (e,k,q) The interpolated electron trapped flux of ELFIN, after aligning with the local maximum of the interpolated electron flux of GPS spacecraft. The displacement in the L direction is provided at the top (f,l,r) Anisotropy coefficient n derived from the comparison of interpolated ELFIN and GPS electron flux.

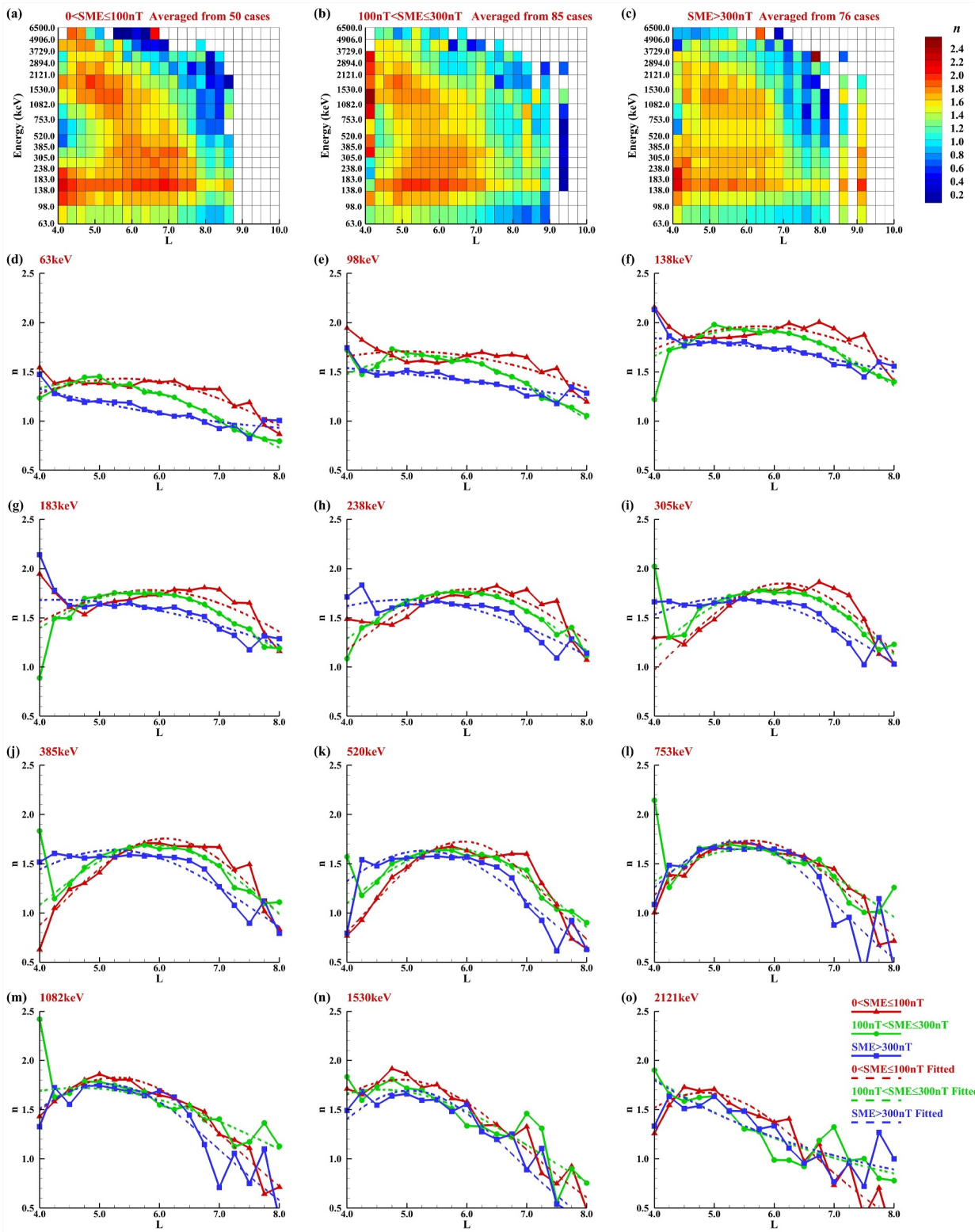

Figure 2. Overview of the anisotropy coefficient n averaged from 211 ELFIN/GPS combined events under different SME indices ($0 < \text{SME} \leq 100$ nT, $100\text{ nT} < \text{SME} \leq 300$ nT and SME > 300 nT) (a–c) Distribution of n at $L = 4 \sim 10$, averaged from 50, 85 and 76 cases respectively under different geomagnetic conditions (d–o) Comparison of data-averaged n and fitted n at different energies and different SME ranges. The solid colored lines depict the variation of data-averaged n at $L = 4 \sim 8$, while the dashed colored lines represent the corresponding fitted lines using fitting function $n(L) = e^{aL^2+bL+c}$, where $0 < L \leq 8$ and a, b, c are the fitting coefficients.

deviation of the linear shift in ELFIN L-shells are -0.55 ± 0.98, -0.47 ± 0.87, and -0.24 ± 0.77 for each respective SME range. Given the limited GPS flux observations beyond $L > 8$ and the sporadic measurements at $L = 4$, the distribution of n around $L = 4$ and $L > 8$ is derived from only a few events (as shown in Figure S4 in Supporting Information S1), leading to greater uncertainties in estimating n. This aspect is also evident in the electron spectra of selected GPS trajectories depicted in Figures S1–S3 in Supporting Information S1. The underestimation of n at 63 keV is also clearly evident in the averaged results. After excluding parameter domains with low confidence in the data, the distribution of n at $4 < L \leq 8$ exhibits weak dependencies on both L and energy. The general energy, L-shell distribution of the anisotropy coefficient n shows a weak anisotropy for large energies at large L-shells, likely partly due to electron scattering by the magnetic field-line curvature (see discussion in Wilkins et al., 2023, and references therein) and by whistler-mode chorus waves outside the plasmasphere (Agapitov et al., 2018; Shi et al., 2016), and also a weak anisotropy within the plasmasphere at L-shells <5 (O'Brien & Moldwin, 2003) for [300, 1000]keV fluxes, likely due to effective scattering of these energies by plasmaspheric hiss waves (e.g., see Ma et al., 2015; Ma et al., 2016; Mourenas et al., 2017). There is also a slight decrease of the anisotropy coefficient n at $L > 6$ during more active geomagnetic conditions, possibly due to more effective electron scattering by intense whistler-mode chorus waves during substorm injections (e.g., see Meredith et al., 2001; Shprits et al., 2007; Agapitov et al., 2018).

Figures 2d–2o depict the comparison of data-averaged n and fitted n at different energies for different SME ranges. The solid colored lines represent the variation of data-averaged n at $L = 4 \sim 8$, while the dashed colored lines indicate the corresponding fitted lines using the fitting function $n(L) = e^{aL^2+bL+c} (4 < L \leq 8)$, where a, b, c are the fitting coefficients and their values at different energies and different SME indices are shown in Table S1 in Supporting Information S1. In general, the trend of n with L shows an initial increase followed by a decrease under different geomagnetic conditions (different SME ranges) at nearly all energies. This pattern suggests that the most anisotropic fluxes are observed within the outer radiation belt, between the plasmapause at $L \approx 5$ and transition region between the outer radiation belt and the plasma sheet at $L \approx 7$. Furthermore, n tends to decrease under higher SME index, a phenomenon particularly noticeable in the region of $L > 5$, suggesting an enhancement of pitch-angle scattering (and isotropization) under more disturbed geomagnetic conditions. However, in the region of $L < 5$, an inverse trend is observed at specific energies, as depicted in Figures 2h–2k. Here, n shows an increase with rising SME index, suggesting formation of highly anisotropic electron populations due to inward radial transport and adiabatic electron heating during substorm injections.

To obtain a more generalized, 2D model of the anisotropy coefficient, we conducted linear fitting of the coefficients a, b, and c with respect to energy. Given the uncertainty in the data-averaged n at several higher energies, we aim to retain as many fitting coefficients a, b, and c of energies as possible and ensure that profiles of fitting coefficients remain monotonic for different SME ranges. Details of the linear fitting of the coefficients a, b, and c are presented in Figure S5 in Supporting Information S1. We retain the fitting coefficients a, b, and c for nine energies. Hence, the fitting function $n(L) = e^{aL^2+bL+c}$ can be reformulated as an energy, L-shell 2D function $n(L,E) = e^{a(E)L^2+b(E)L+c(E)}$, where $a(E)$, $b(E)$, and $c(E)$ represent the energy-related coefficients and their linear fitting coefficients a_1, a_2, b_1, b_2, c_1, c_2 are shown in Table S2 in Supporting Information S1.

Figures 3a–3l illustrate the comparison between n averaged over ELFIN/GPS combined events (represented by solid colored lines) and $n(L,E)$ predicted by the energy, L-shell 2D functions (represented by dashed colored lines) at 12 energies for different SME levels. The comparison yields satisfactory results for the first nine energy channels. However, for energies exceeding 1 MeV, $n(L,E)$ deviates significantly from the data-averaged n, indicating the need for further refinement of the model to accurately capture the n behavior at such relativistic energies. Nevertheless, the underestimation of n at 63 keV is partially corrected by $n(L,E)$, suggesting that the model smooth some of the discrepancies observed in the data. This underscores the potential for refining the $n(L,E)$ model to enhance its accuracy.

Figures 3m–3o provide an overview of the distribution of our two-dimensional model $n(L,E)$ at $L = 4 \sim 10$ for different SME ranges, spanning from 63 to 2,121 keV. Although the model was not specifically considered for $L = 8 \sim 10$, we extend our predictions to this range to offer a more comprehensive analysis. Indeed, the trend of $n(L,E)$ with respect to L reveals an intriguing behavior characterized by a L-shell localized maximum of the anisotropy coefficient within the outer radiation belt. The position of this localized maximum in L tends to migrate toward lower L-shells as SME index elevates, underscoring the profound impact of geomagnetic activity on the compression of the inner magnetosphere. Moreover, it is noteworthy that the local maximum $n(L,E)$ tends to

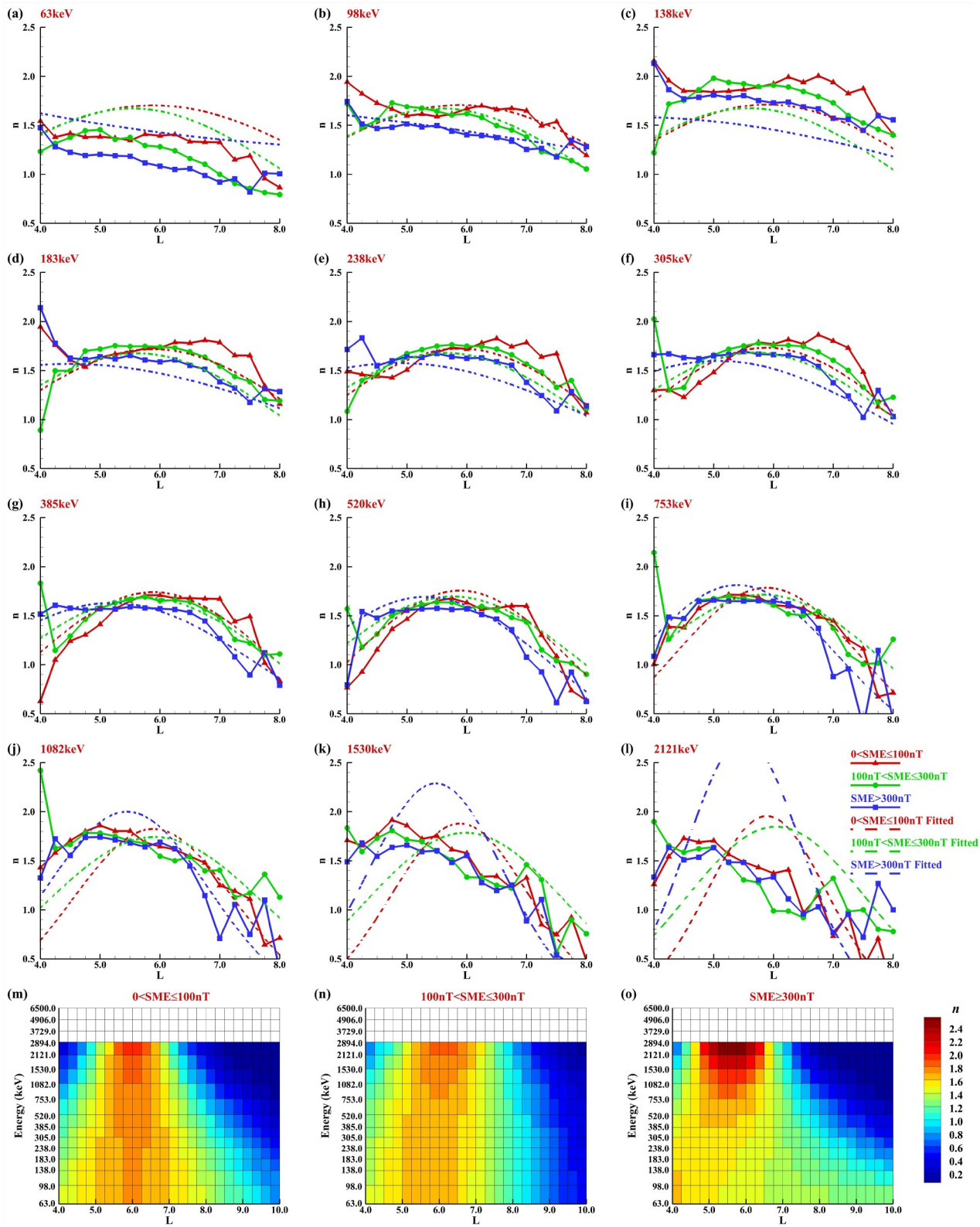

Figure 3. Comparison of n averaged from ELFIN/GPS combined events and $n(L,E)$ predicted by the energy, L-related functions at 12 energies under different SME indices (a–l) The solid and dashed colored lines represent the data-averaged n and 2D-model-derived $n(L,E)$ at $L = 4 \sim 8$ under different SME indices, respectively (m–o) Distribution of 2D-model-derived $n(L,E)$ at $L = 4 \sim 10$ from 63 to 2121 keV under different SME indices.

exhibit an increasing trend with energy. This trend becomes particularly evident when comparing higher energy levels, where the variations in the local maxima are more pronounced. This pattern suggests a weakened propensity for pitch-angle scattering or stronger anisotropic (adiabatic) heating at higher energies. Thus higher energy electrons likely experience less scattering and more efficient acceleration, what changes the $n(L,E)$ distribution. Conversely, as the SME index increases, there is typically a slight diminution in the local maximum $n(L,E)$, suggestive of a stronger pitch-angle scattering under more disturbed geomagnetic conditions. Note that the 2D $n(L,E)$ model provides a simplified n distribution without a n maximum at >2MeV range, and this n minimum at intermediate energies is not localized in energies (compare Figures 2a–2c and 3m-mo).

4. ELFIN/Arase Model Verification

To validate the proposed model of anisotropy coefficient, we compare ELFIN measurements with those provided by Arase MEPe and HEP-L instruments: the low-altitude ELFIN data are projected to Arase latitudes using 1D, $n(L)$, and 2D, $n(E,L)$, models, and then compared with direct Arase measurements. Based on the averaged δL as discussed in Section 2, we use -0.5, -0.5, and -0.25 as the representative values for each range of geomagnetic activity to characterize the uncertainty of ELFIN mapping. Figure 4 presents a typical ELFIN/Arase combined event, where the maxima of the one-hour SME index preceding the ELFIN trajectory fall within the range of 0–100 nT. Figure 4a displays the combined electron spectra from MEPe and HEP-L onboard Arase on 30 April 2020 at $L = 4 \sim 7$, with time interval of measurements indicated at the top. Since the lowest energy channel of HEP-L overlaps with MEPe, we substituted the flux of HEP-L's lowest energy channel (60.2 keV) with the flux of MEPe's 60.4 keV energy channel. Figure 4b displays the electron trapped flux of the corresponding ELFIN-A trajectory, which has been adjusted by the averaged δL, occurring approximately 2 hr after the Arase event. The duration of the ELFIN-A trajectory is also indicated at the top. In Figure 4c, SME SMU and SML indices preceding the ELFIN trajectory are displayed, with the Arase and ELFIN measurement intervals highlighted by the orange and pink dashed rectangle, respectively. Figure 4d shows the interpolated electron flux of Arase HEP-L with the same energy resolution as ELFIN-A. Since the maximum energy of Arase HEP-L is 1,590.8 keV, we refrain from extrapolating and thus only perform interpolation for the 11 corresponding energy levels of ELFIN.

Consequently, the predicted Arase electron spectra depicted in Figures 4e and 4f are obtained by projecting the electron flux observed at ELFIN-A altitude to Arase altitude using Equation 4, with Figure 4e utilizing the one-dimensional model $n(L)$ and Figure 4f utilizing the two-dimensional model $n(L,E)$. Figure 4g shows the scatter plot comparison of the Arase electron flux and ELFIN-projected electron flux at the first 10 energies. In each panel, the solid colored line with triangle symbols represents the Arase electron flux, while the dashed line with circle symbols and dotted colored line with square symbols represent the ELFIN-projected electron flux using one-dimensional (1D) model $n(L)$ and two-dimensional (2D) model $n(L,E)$, respectively. In each panel, we calculate the median symmetric accuracy (ζ) (Morley et al., 2018) and the symmetric signed percentage bias (SSPB) (Morley et al., 2018) for both 1D model $n(L)$ and 2D model $n(L,E)$, which focus on relative errors and percentage errors, providing a more robust and interpretable assessment of model performance. ζ offers a measure of accuracy that remains consistent even with varying data scales, while the SSPB effectively highlights the direction and magnitude of bias in the model predictions. These metrics prove to be reliable tools for evaluating and comparing the performance of the 1D model in predicting electron fluxes (Morley et al., 2018). For 63 keV energy in Figure 4g, ζ_{1d} of 41.34% and SSPB_{1d} of -35.57% indicate that half of the forecast errors are smaller than a factor of 1.41, and the median forecast error underestimates by 35.57%; ζ_{2d} of 29.02% and SSPB_{2d} of 28.06% suggest that half of the forecast errors are smaller than a factor of 1.29, and the median forecast error overestimates by 28.06%, and so forth. In general, both the 1D-model-derived electron flux and 2D-model-derived electron flux closely align with each other and match the electron flux observed by Arase in Figure 4g. The largest forecast errors for the 1D model $n(L)$ and the 2D model $n(L,E)$ come from the 183 and 1,082 keV energies, with errors of $\zeta_{1d} = 190.66\%$ and $\zeta_{2d} = 146.96\%$, respectively. Despite these high values, they still indicate that half of the forecast errors are smaller than a factor of 3, which is far less than one order of magnitude. Notably, even at energies greater than 1 MeV, the 2D model provides predictions that closely resemble those of the 1D model and match the Arase observations to a satisfactory extent. The magnitude of Arase/ELFIN discrepancies maximizes at large L, where uncertainties of ELFIN mapping to Arase latitudes are expected to be larger. Further details about the performance metrics of the 1D and 2D models can be found in Figure S6a in Supporting Information S1. This agreement between model predictions and observations

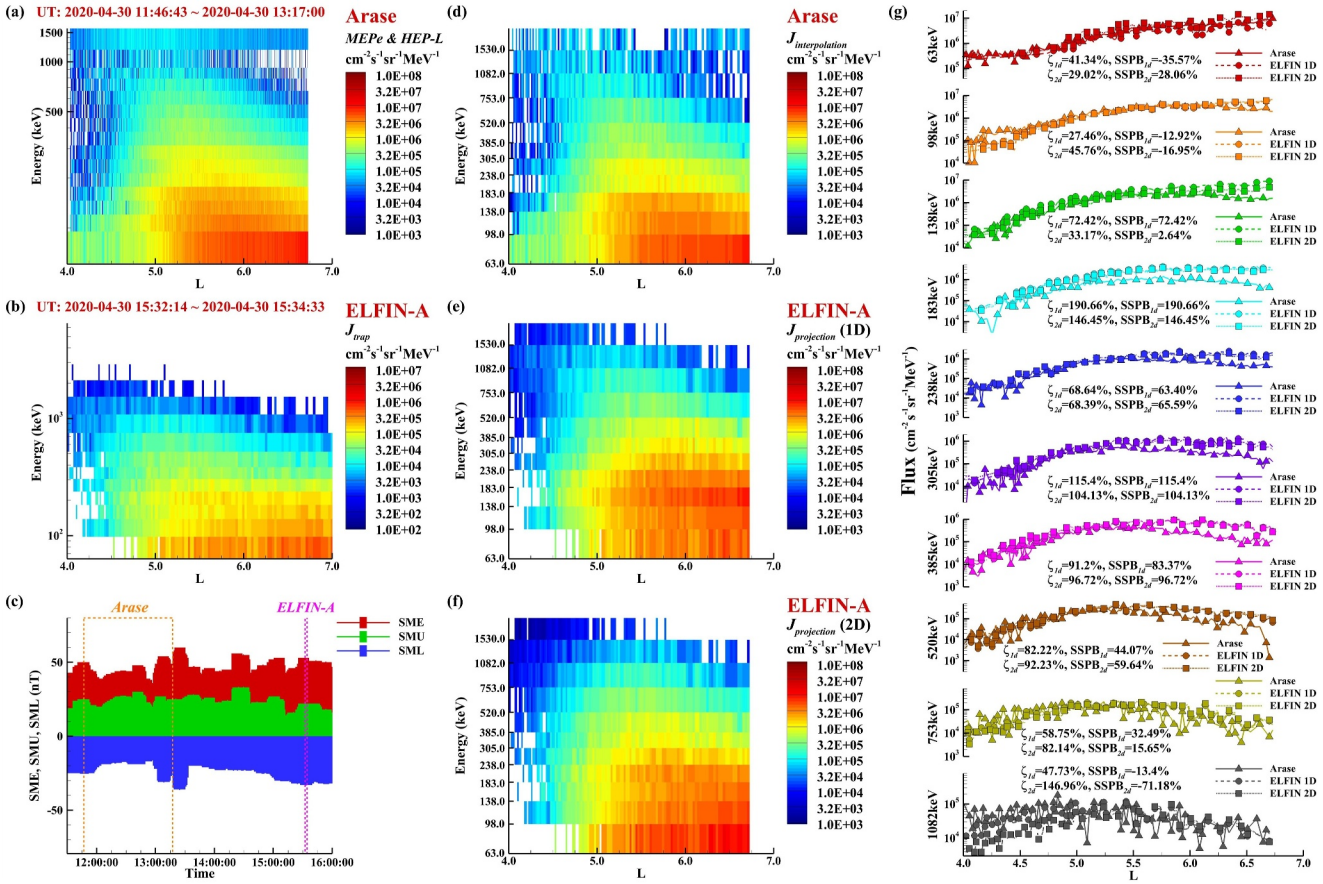

Figure 4. Overview of an ELFIN/Arase combined event categorized for $0 < \text{SME} \leq 100$ nT. (a) Electron flux from MEPe and HEP-L on board Arase on 30 April 2020 at $L = 4 \sim 7$. (b) Trapped electron flux during the ELFIN-A trajectory, adjusted by the average linear shift of ELFIN L-shells, occurring roughly 2 hr after the corresponding Arase event. (c) SuperMAG SME SMU and SML indices of the ELFIN/Arase combined event. (d) Interpolated electron flux of Arase HEP-L with the same energy resolution as ELFIN-A. (e) The predicted Arase electron flux using the one-dimensional model $n(L, E)$ to project the electron flux observed at ELFIN-A altitude to Arase altitude. (f) The predicted Arase electron flux using the two-dimensional model $n(L, E)$ to project the electron flux observed at ELFIN-A altitude to Arase altitude. (g) Comparisons of Arase electron flux and ELFIN-projected electron flux for 10 energies at $L = 4 \sim 7$. In each panel, the solid colored line with triangle symbols represents the Arase electron flux, while the dashed line with circle symbols and dotted colored line with square symbols represent the ELFIN-projected electron flux using one-dimensional model $n(L)$ and two-dimensional model $n(L, E)$ respectively. In each panel, we calculate the median symmetric accuracy (ζ) and the symmetric signed percentage bias (SSPB) for both 1D model $n(L)$ and 2D model $n(L, E)$.

underscores the accuracy and reliability of both the 1D and 2D models in estimating electron pitch-angle scattering in this region.

Figures 5 and 6 illustrate two additional ELFIN/Arase combined events categorized based on the maximum of the one-hour SME index preceding the ELFIN trajectory. In Figure 5, the SME index falls within the range of 100–300 nT, while in Figure 6, it exceeds 300 nT, indicating highly disturbed geomagnetic conditions. For both events, we employ the 1D model $n(L)$ and the 2D model $n(L, E)$ to project the electron flux observed at ELFIN-A altitude to Arase altitude. The electron spectra derived from the 1D model $n(L)$ and 2D model $n(L, E)$ are displayed in Figures 5e and 5f, as well as Figures 6e and 6f, respectively. Figures 5g and 6g illustrate the scatter plot comparisons between the electron flux measured by Arase and that projected from ELFIN. It is worth noting that the forecast errors are typically more pronounced in the lowest energy panel of Figures 5g and 6g, where the projected electron fluxes derived from both the 1D and 2D models tend to be smaller than the observed Arase electron flux. This discrepancy is attributed to the underestimation of n at 63 keV, as previously discussed. However, despite this discrepancy, the error does not exceed one order of magnitude. Furthermore, the 2D model, by correcting n to some extent, yields a flux mapping notably closer to the Arase measurement compared to the 1D model. At energies below 1 MeV, both the 1D and 2D model-derived fluxes closely match the observations from Arase, indicating the efficacy of both modeling approaches in capturing electron dynamics. However, as energy levels

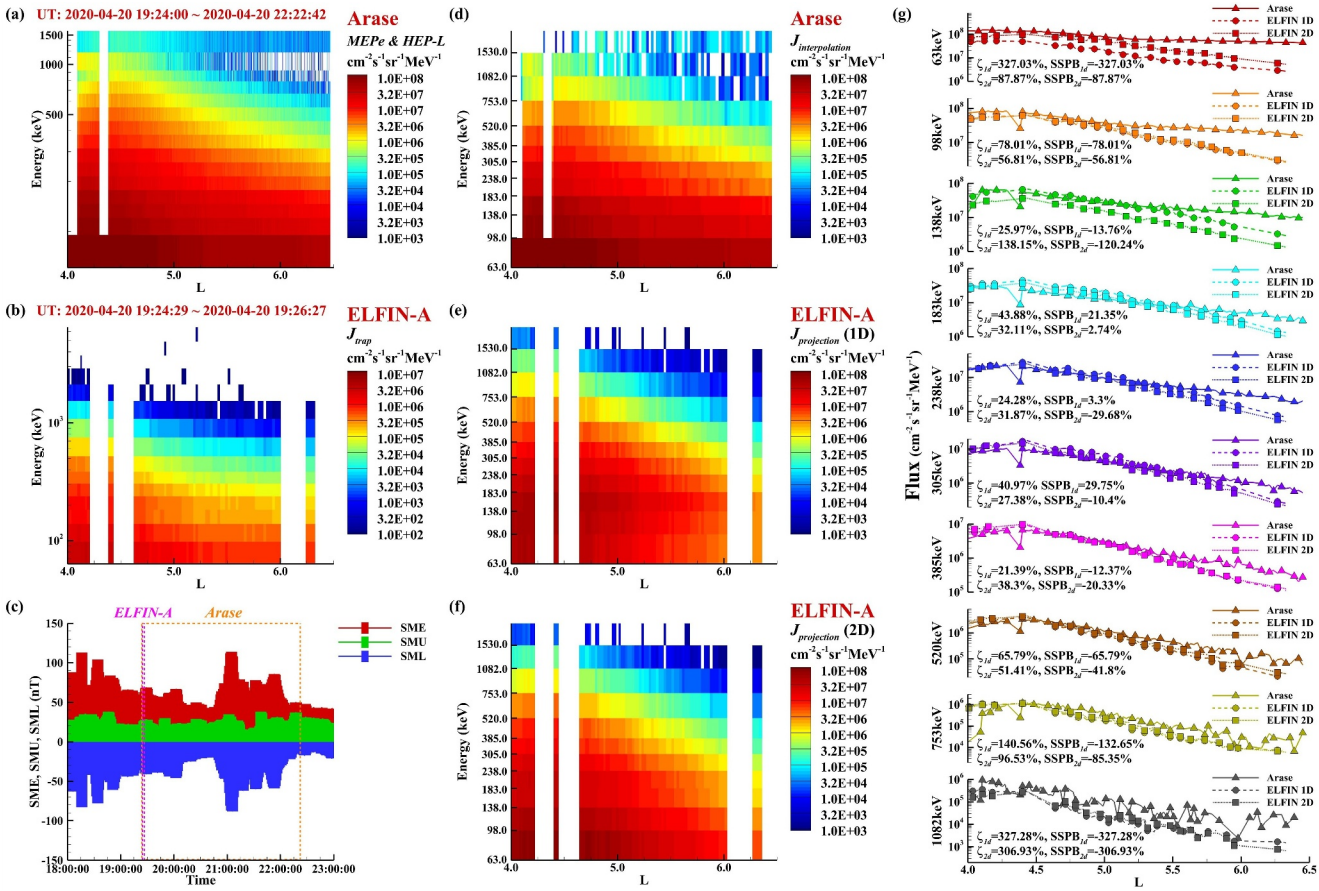

Figure 5. Overview of an ELFIN/Arase combined event categorized for 100 nT < SME ≤ 300 nT, organized as the same format as Figure 4.

surpass 1 MeV, the discrepancy between the predicted fluxes and Arase measurements becomes more pronounced in Figure 5g. Further details about the performance metrics of the 1D and 2D models can be found in Figures S6b and S6c in Supporting Information S1. Note that at $L \sim 4$ we do not have sufficient GPS measurements in our GPS/ELFIN flux comparison, and within this L-shell range our model may not sufficiently accurately describe energy, L-shell flux distribution: the model shows a flux decrease to smaller L at all energies and misses possible effects of ≥1MeV flux enhancements there.

5. Discussion and Conclusions

In this paper, we develop a model of the electron anisotropy coefficient, n, allowing the phase space mapping of low-altitude ELFIN measurements of energetic electron fluxes to the equatorial plane. Such mapping technique should provide a new opportunity for tracing the meso-scale dynamic variations (transients) of energetic electron fluxes in the outer radiation belt, for example, plasma sheet injections (e.g., Califf et al., 2022; Lejosne et al., 2018; Turner, Claudepierre, et al., 2015; Turner et al., 2017), because ELFIN measurements provide an almost instantaneous snapshot of the entire inner magnetosphere. Our model further develops the idea of radiation belt monitoring from low altitudes, originally proposed in Allison et al. (2018); Claudepierre and O'Brien (2020) for POES data. Moreover, the same model, with some modifications accounting for difference in field-of-view of different energetic particle detectors, can be adapted for new CubeSat missions, like CIRBE (Li, 2024; Li et al., 2024), and the forthcoming REAL (Millan et al., 2021, 2022).

The proposed model of n coefficient is presented in two formats: for any energy of one of ELFIN energy channels there is a 1D model of $n(L,AE)$, whereas for energies below 1 MeV such 1D models are merged into a 2D model of $n(E,L,AE)$. Model verification with Arase energetic electron measurements demonstrate that ELFIN spectra,

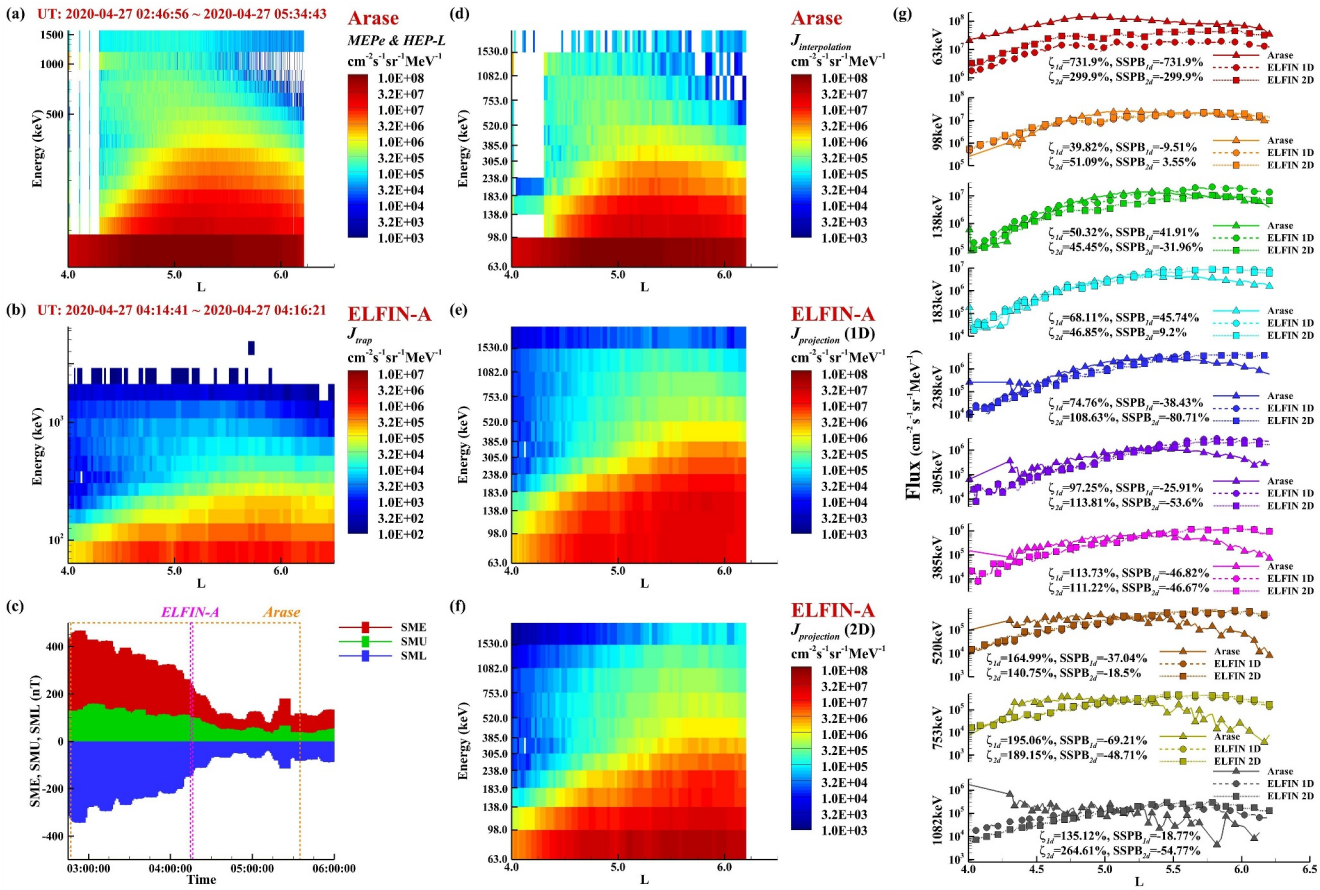

Figure 6. Overview of an ELFIN/Arase combined event categorized for SME > 300 nT, organized as the same format as Figure 4.

properly projected to Arase latitudes, can well describe Arase measurements. Note that the proposed model works only for anisotropic electron fluxes in the outer radiation belt and does not describe isotropic electron populations in the plasma sheet. Therefore, for further model improvement, it could be useful to determine the inner (equatorward) boundary of electron isotropic precipitation, the so-called isotropy boundary (Sergeev et al., 2012; Wilkins et al., 2023). Such model of isotropy boundary as a function of energy and geomagnetic activity could be combined with the model of electron anisotropy coefficient, n, to provide more accurate electron flux mapping to radiation belts and plasma sheet.

Data Availability Statement

ELFIN data is available at http://themis-data.igpp.ucla.edu/ela/. The v1.10 public release of GPS CXD data is available at https://data.noaa.gov/onestop/collections/details/3560e232-7fd0-4fd9-aee2-8b4adcd47ffa. Science data of the Arase (ERG) satellite were obtained from the Arase Science Center operated by ISAS/JAXA and ISEE/Nagoya University (https://ergsc.isee.nagoya-u.ac.jp/index.shtml.en, Miyoshi, Shinohara, and Jun (2018)). The present study analyzed the HEP L2_v03_01 data (Mitani, Hori, et al., 2018), MEP-e L2_v01_02 data (Kasahara, Yokota, Mitani, et al., 2018), MGF L2_v04_04 data (Matsuoka et al., 2018) and Orbit L3_v02 data (Miyoshi, Shinohara, et al., 2018). Data was retrieved and analyzed using PySPEDAS and SPEDAS, see Angelopoulos et al. (2019).

Acknowledgments
A.V.A., X.J.Z., and V.A. acknowledge support by NASA awards 80NSSC20K1270, 80NSSC23K0403, 80NSSC24K0558, NAS5-02099, and NSF grants AGS-1242918, AGS-2019950, and AGS-2021749. We are grateful to NASA's CubeSat Launch Initiative for ELFIN's successful launch. We acknowledge early support of the ELFIN project by the AFOSR, under its University Nanosat Program; by the UNP-8 project, contract FA9453-12-D-0285; and by the California Space Grant program. We sincerely acknowledge the critical contributions of the numerous volunteer ELFIN team student members. Contributions by S.K.M. were supported by the U.S. Department of Energy through the Los Alamos National Laboratory. Los Alamos National Laboratory is operated by Triad National Security, LLC, for the National Nuclear Security Administration of the U.S. Department of Energy (Contract No. 89233218CNA000001). We thank the CXD team at Los Alamos National Laboratory for providing the LANL-GPS energetic particle data.

References

Agapitov, O. V., Mourenas, D., Artemyev, A. V., Mozer, F. S., Hospodarsky, G., Bonnell, J., & Krasnoselskikh, V. (2018). Synthetic empirical chorus wave model from combined van allen Probes and cluster statistics. *Journal of Geophysical Research (Space Physics)*, *123*(1), 297–314. https://doi.org/10.1002/2017JA024843

Allison, H. J., Horne, R. B., Glauert, S. A., & Del Zanna, G. (2018). Determination of the equatorial electron differential flux from observations at low earth orbit. *Journal of Geophysical Research (Space Physics)*, *123*(11), 9574–9596. https://doi.org/10.1029/2018JA025786

Allison, H. J., Shprits, Y. Y., Zhelavskaya, I. S., Wang, D., & Smirnov, A. G. (2021). Gyroresonant wave-particle interactions with chorus waves during extreme depletions of plasma density in the Van Allen radiation belts. *Science Advances*, *7*(5), eabc0380. https://doi.org/10.1126/sciadv.abc0380

Angelopoulos, V., Cruce, P., Drozdov, A., Grimes, E. W., Hatzigeorgiu, N., King, D. A., et al. (2019). The space physics environment data analysis system (SPEDAS). *Space Science Reviews*, *215*(1), 9. https://doi.org/10.1007/s11214-018-0576-4

Angelopoulos, V., Tsai, E., Bingley, L., Shaffer, C., Turner, D. L., Runov, A., et al. (2020). The ELFIN mission. *Space Science Reviews*, *216*(5), 103. https://doi.org/10.1007/s11214-020-00721-7

Angelopoulos, V., Zhang, X. J., Artemyev, A. V., Mourenas, D., Tsai, E., Wilkins, C., et al. (2023). Energetic electron precipitation driven by electromagnetic ion cyclotron waves from ELFIN's low altitude perspective. *Space Science Reviews*, *219*(5), 37. https://doi.org/10.1007/s11214-023-00984-w

Artemyev, A. V., Angelopoulos, V., Zhang, X. J., Runov, A., Petrukovich, A., Nakamura, R., et al. (2022). Thinning of the magnetotail current sheet inferred from low-altitude observations of energetic electrons. *Journal of Geophysical Research (Space Physics)*, *127*(10), e2022JA030705. https://doi.org/10.1029/2022JA030705

Artemyev, A. V., Zhang, X. J., Demekhov, A. G., Meng, X., Angelopoulos, V., & Fedorenko, Y. V. (2024). Relativistic electron precipitation driven by mesoscale transients, inferred from ground and multi-spacecraft platforms. *Journal of Geophysical Research (Space Physics)*, *129*(2), e2023JA032287. https://doi.org/10.1029/2023JA032287

Botek, E., Pierrard, V., & Winant, A. (2023). Prediction of radiation belts electron fluxes at a low earth orbit using neural networks with PROBA-V/EPT data. *Space Weather*, *21*(7), e2023SW003466. https://doi.org/10.1029/2023SW003466

Boyd, A. J., Green, J. C., O'Brien, T. P., & Claudepierre, S. G. (2023). Specifying high altitude electrons using low-altitude LEO systems: Updates to the SHELLS model. *Space Weather*, *21*(3), e2022SW003338. https://doi.org/10.1029/2022SW003338

Boynton, R. J., Mourenas, D., & Balikhin, M. A. (2017). Electron flux dropouts at L\sim 4.2 from global positioning system satellites: Occurrences, magnitudes, and main driving factors. *Journal of Geophysical Research (Space Physics)*, *122*, 11. https://doi.org/10.1002/2017JA024523

Califf, S., Zhao, H., Gkioulidou, M., Manweiler, J. W., Mitchell, D. G., & Tian, S. (2022). Multi-event study on the connection between subauroral polarization streams and deep energetic particle injections in the inner magnetosphere. *Journal of Geophysical Research (Space Physics)*, *127*(2), e2021JA029895. https://doi.org/10.1029/2021JA029895

Capannolo, L., Li, W., Ma, Q., Qin, M., Shen, X. C., Angelopoulos, V., et al. (2023). Electron precipitation observed by ELFIN using proton precipitation as a proxy for electromagnetic ion cyclotron (EMIC) waves. *Geophysical Research Letters*, *50*(21), e2023GL103519. https://doi.org/10.1029/2023GL103519

Carver, M., Morley, S. K., & Stricklan, A. (2020). GPS constellation energetic particle measurements. *IEEE Aerospace Conference*, 1–10. https://doi.org/10.1109/AERO47225.2020.9172652

Chen, Y., Friedel, R. H. W., Henderson, M. G., Claudepierre, S. G., Morley, S. K., & Spence, H. E. (2014). Repad: An empirical model of pitch angle distributions for energetic electrons in the Earth's outer radiation belt. *Journal of Geophysical Research (Space Physics)*, *119*(3), 1693–1708. https://doi.org/10.1002/2013JA019431

Claudepierre, S. G., & O'Brien, T. P. (2020). Specifying high-altitude electrons using low-altitude LEO systems: The SHELLS model. *Space Weather*, *18*(3), e02402. https://doi.org/10.1029/2019SW002402

Drozdov, A. Y., Kondrashov, D., Strounine, K., & Shprits, Y. Y. (2023). Reconstruction of electron radiation belts using data assimilation and machine learning. *Frontiers in Astronomy and Space Sciences*, *10*, 1072795. https://doi.org/10.3389/fspas.2023.1072795

Evans, D. S., & Greer, M. S. (2004). Polar orbiting environmental satellite space environment monitor-2: Instrument description and archive data documentation.

Gabrielse, C., Angelopoulos, V., Runov, A., & Turner, D. L. (2014). Statistical characteristics of particle injections throughout the equatorial magnetotail. *Journal of Geophysical Research*, *119*(4), 2512–2535. https://doi.org/10.1002/2013JA019638

Gabrielse, C., Spanswick, E., Artemyev, A., Nishimura, Y., Runov, A., Lyons, L., et al. (2019). Utilizing the heliophysics/geospace system observatory to understand particle injections: Their scale sizes and propagation directions. *Journal of Geophysical Research (Space Physics)*, *124*(7), 5584–5609. https://doi.org/10.1029/2018JA025588

Gannon, J. L., Li, X., & Heynderickx, D. (2007). Pitch angle distribution analysis of radiation belt electrons based on Combined Release and Radiation Effects Satellite Medium Electrons A data. *Journal of Geophysical Research*, *112*(A5), 5212. https://doi.org/10.1029/2005JA011565

Ginisty, F., Wrobel, F., Ecoffet, R., Standarovski, D., Mekki, J., Ruffenach, M., et al. (2023). CARMEN 2 and 3 LEO electron flux measurements linear projection onto RBSP elliptical orbit. *IEEE Transactions on Nuclear Science*, *70*(8), 1564–1571. https://doi.org/10.1109/TNS.2023.3260904

Gjerloev, J. W. (2012). The SuperMAG data processing technique. *Journal of Geophysical Research (Space Physics)*, *117*(A9), A09213. https://doi.org/10.1029/2012JA017683

Horne, R. B., Glauert, S. A., Meredith, N. P., Boscher, D., Maget, V., Heynderickx, D., & Pitchford, D. (2013). Space weather impacts on satellites and forecasting the Earth's electron radiation belts with SPACECAST. *Space Weather*, *11*(4), 169–186. https://doi.org/10.1002/swe.20023

Kasahara, S., Yokota, S., Hori, T., Keika, K., Miyoshi, Y., & Shinohara, I. (2018a). Exploration of energization and radiation in geospace (erg) mep-e level-2 omniflux data. Version 01_02. *ERG Science Center, Institute for Space-Earth Environmental Research, Nagoya*. https://doi.org/10.34515/DATA.ERG-02001

Kasahara, S., Yokota, S., Mitani, T., Asamura, K., Hirahara, M., Shibano, Y., & Takashima, T. (2018b). Medium-energy particle experiments-electron analyzer (MEP-e) for the exploration of energization and radiation in geospace (ERG) mission. *Earth Planets and Space*, *70*(1), 69. https://doi.org/10.1186/s40623-018-0847-z

Lejosne, S., Kunduri, B. S. R., Mozer, F. S., & Turner, D. L. (2018). Energetic electron injections deep into the inner magnetosphere: A result of the subauroral polarization stream (saps) potential drop. *Geophysical Research Letters*, *45*(9), 3811–3819. https://doi.org/10.1029/2018GL077969

Li, W., Thorne, R. M., Ma, Q., Ni, B., Bortnik, J., Baker, D. N., et al. (2014). Radiation belt electron acceleration by chorus waves during the 17 March 2013 storm. *Journal of Geophysical Research*, *119*(6), 4681–4693. https://doi.org/10.1002/2014JA019945

Li, X. (2024). Unveiling energetic particle dynamics in the near-earth environment from cubesat missions. *AGU Advances*, *5*(3), e2024AV001256. https://doi.org/10.1029/2024AV001256

Li, X., Selesnick, R., Mei, Y., O'Brien, D., Hogan, B., Xiang, Z., et al. (2024). First results from reptile-2 measurements onboard cirbe. *Geophysical Research Letters*, *51*(3), e2023GL107521. https://doi.org/10.1029/2023GL107521

Ma, Q., Li, W., Bortnik, J., Thorne, R. M., Chu, X., Ozeke, L. G., et al. (2018). Quantitative evaluation of radial diffusion and local acceleration processes during GEM challenge events. *Journal of Geophysical Research (Space Physics)*, *123*(3), 1938–1952. https://doi.org/10.1002/2017JA025114

Ma, Q., Li, W., Thorne, R. M., Bortnik, J., Reeves, G. D., Kletzing, C. A., et al. (2016). Characteristic energy range of electron scattering due to plasmaspheric hiss. *Journal of Geophysical Research*, *121*(12), 11. https://doi.org/10.1002/2016JA023311

Ma, Q., Li, W., Thorne, R. M., Ni, B., Kletzing, C. A., Kurth, W. S., et al. (2015). Modeling inward diffusion and slow decay of energetic electrons in the Earth's outer radiation belt. *Geophysical Research Letters*, *42*(4), 987–995. https://doi.org/10.1002/2014GL062977

Matsuoka, A., Teramoto, M., Imajo, S., Kurita, S., Miyoshi, Y., & Shinohara, I. (2018). The mgf instrument level-2 high-resolution magnetic field data of exploration of energization and radiation in geospace (erg) arase satellite. Version 04_04. *ERG Science Center, Institute for Space-Earth Environmental Research, Nagoya*. https://doi.org/10.34515/DATA.ERG-06000

Mauk, B. H., Fox, N. J., Kanekal, S. G., Kessel, R. L., Sibeck, D. G., & Ukhorskiy, A. (2013). Science objectives and rationale for the radiation belt storm Probes mission. *Space Science Reviews*, *179*(1–4), 3–27. https://doi.org/10.1007/s11214-012-9908-y

Meredith, N. P., Horne, R. B., & Anderson, R. R. (2001). Substorm dependence of chorus amplitudes: Implications for the acceleration of electrons to relativistic energies. *Journal of Geophysical Research*, *106*(A7), 13165–13178. https://doi.org/10.1029/2000JA900156

Millan, R., Sample, J., Sotirelis, T., McCarthy, M., Woodger, L., Shih, A. Y., et al. (2022). New missions for understanding electron microburst precipitation. *44th cospar scientific assembly*, *44*, 3327. held 16-24 july.

Millan, R., Sample, J., Sotirelis, T., Woodger, L., Li, W., Capannolo, L., & Cantwell, K. (2021). The relativistic electron atmospheric loss CubeSat. *Agu Fall Meeting Abstracts*, *2021*, SM55D–1810.

Mitani, T., Hori, T., Park, I., Takashima, T., Miyoshi, Y., & Shinohara, I. (2018). The hep instrument level-2 omni-directional flux data of exploration of energization and radiation in geospace (erg) arase satellite. Version 03_01. *ERG Science Center, Institute for Space-Earth Environmental Research, Nagoya*. https://doi.org/10.34515/DATA.ERG-01001

Mitani, T., Takashima, T., Kasahara, S., Miyake, W., & Hirahara, M. (2018). High-energy electron experiments (HEP) aboard the ERG (Arase) satellite. *Earth Planets and Space*, *70*(1), 77. https://doi.org/10.1186/s40623-018-0853-1

Miyoshi, Y., Hori, T., Shoji, M., Teramoto, M., Chang, T. F., Segawa, T., et al. (2018). The ERG science center. *Earth Planets and Space*, *70*(1), 96. https://doi.org/10.1186/s40623-018-0867-8

Miyoshi, Y., Shinohara, I., & Jun, C.-W. (2018). Exploration of energization and radiation in geospace (erg) orbit level-3 data. Version 02. *ERG Science Center, Institute for Space-Earth Environmental Research, Nagoya*. https://doi.org/10.34515/DATA.ERG-12001

Miyoshi, Y., Shinohara, I., Takashima, T., Asamura, K., Higashio, N., Mitani, T., et al. (2018). Geospace exploration project ERG. *Earth Planets and Space*, *70*(1), 101. https://doi.org/10.1186/s40623-018-0862-0

Morley, S. K., Brito, T. V., & Welling, D. T. (2018). Measures of model performance based on the log accuracy ratio. *Space Weather*, *16*(1), 69–88. Retrieved from https://doi.org/10.1002/2017SW001669

Morley, S. K., Friedel, R. H. W., Cayton, T. E., & Noveroske, E. (2010a). A rapid, global and prolonged electron radiation belt dropout observed with the Global Positioning System constellation. *Geophysical Research Letters*, *37*(6), 6102. https://doi.org/10.1029/2010GL042772

Morley, S. K., Friedel, R. H. W., Spanswick, E. L., Reeves, G. D., Steinberg, J. T., Koller, J., et al. (2010b). Dropouts of the outer electron radiation belt in response to solar wind stream interfaces: Global positioning system observations. *Royal Society of London Proceedings Series A*, *466*(2123), 3329–3350. https://doi.org/10.1098/rspa.2010.0078

Morley, S. K., Sullivan, J. P., Carver, M. R., Kippen, R. M., Friedel, R. H. W., Reeves, G. D., & Henderson, M. G. (2017). Energetic particle data from the global positioning system constellation. *Space Weather*, *15*(2), 283–289. https://doi.org/10.1002/2017SW001604

Morley, S. K., Sullivan, J. P., Henderson, M. G., Blake, J. B., & Baker, D. N. (2016). The Global Positioning System constellation as a space weather monitor: Comparison of electron measurements with Van Allen Probes data. *Space Weather*, *14*(2), 76–92. https://doi.org/10.1002/2015SW001339

Mourenas, D., Artemyev, A. V., Zhang, X. J., Angelopoulos, V., Tsai, E., & Wilkins, C. (2021). Electron lifetimes and diffusion rates inferred from ELFIN measurements at low altitude: First results. *Journal of Geophysical Research (Space Physics)*, *126*(11), e29757. https://doi.org/10.1029/2021JA029757

Mourenas, D., Ma, Q., Artemyev, A. V., & Li, W. (2017). Scaling laws for the inner structure of the radiation belts. *Geophysical Research Letters*, *44*(7), 3009–3018. https://doi.org/10.1002/2017GL072987

O'Brien, T. P., & Moldwin, M. B. (2003). Empirical plasmapause models from magnetic indices. *Geophysical Research Letters*, *30*(4), 1152. https://doi.org/10.1029/2002GL016007

Olifer, L., Morley, S. K., Ozeke, L. G., Mann, I. R., Kalliokoski, M. M. H., Henderson, M. G., et al. (2024). Rapid acceleration bursts in the van allen radiation belt. *Journal of Geophysical Research (Space Physics)*, *129*(5), e2024JA032544. https://doi.org/10.1029/2024JA032544

Roederer, J. G. (1970). Dynamics of geomagnetically trapped radiation.

Sergeev, V. A., Nishimura, Y., Kubyshkina, M., Angelopoulos, V., Nakamura, R., & Singer, H. (2012). Magnetospheric location of the equatorward prebreakup arc. *Journal of Geophysical Research (Space Physics)*, *117*(A1), A01212. https://doi.org/10.1029/2011JA017154

Shi, R., Summers, D., Ni, B., Fennell, J. F., Blake, J. B., Spence, H. E., & Reeves, G. D. (2016). Survey of radiation belt energetic electron pitch angle distributions based on the Van Allen Probes MagEIS measurements. *Journal of Geophysical Research (Space Physics)*, *121*(2), 1078–1090. https://doi.org/10.1002/2015JA021724

Shprits, Y. Y., Meredith, N. P., & Thorne, R. M. (2007). Parameterization of radiation belt electron loss timescales due to interactions with chorus waves. *Geophysical Research Letters*, *34*(11), 11110. https://doi.org/10.1029/2006GL029050

Smirnov, A. G., Berrendorf, M., Shprits, Y. Y., Kronberg, E. A., Allison, H. J., Aseev, N. A., et al. (2020). Medium energy electron flux in Earth's outer radiation belt (merlin): A machine learning model. *Space Weather*, *18*(11), e02532. https://doi.org/10.1029/2020SW002532

Thorne, R. M., Li, W., Ni, B., Ma, Q., Bortnik, J., Chen, L., et al. (2013). Rapid local acceleration of relativistic radiation-belt electrons by magnetospheric chorus. *Nature*, *504*(7480), 411–414. https://doi.org/10.1038/nature12889

Tsai, E., Palla, A., Norris, A., King, J., Russell, C., Ye, S., et al. (2024). Remote sensing of electron precipitation mechanisms enabled by ELFIN mission operations and ADCS design. *Engineering Archive*. https://doi.org/10.31224/3487

Tsyganenko, N. A. (1989). A magnetospheric magnetic field model with a warped tail current sheet. *Planatary Space Science*, *37*(1), 5–20. https://doi.org/10.1016/0032-0633(89)90066-4

Tu, W., Cunningham, G. S., Chen, Y., Morley, S. K., Reeves, G. D., Blake, J. B., et al. (2014). Event-specific chorus wave and electron seed population models in DREAM3D using the Van Allen Probes. *Geophysical Research Letters*, *41*(5), 1359–1366. https://doi.org/10.1002/2013GL058819

Turner, D. L., Claudepierre, S. G., Fennell, J. F., O'Brien, T. P., Blake, J. B., Lemon, C., et al. (2015). Energetic electron injections deep into the inner magnetosphere associated with substorm activity. *Geophysical Research Letters*, *42*(7), 2079–2087. https://doi.org/10.1002/2015GL063225

Turner, D. L., Fennell, J. F., Blake, J. B., Claudepierre, S. G., Clemmons, J. H., Jaynes, A. N., et al. (2017). Multipoint observations of energetic particle injections and substorm activity during a conjunction between magnetospheric multiscale (MMS) and van allen Probes. *Journal of Geophysical Research (Space Physics)*, *122*(11), 11481–11504. https://doi.org/10.1002/2017JA024554

Turner, D. L., O'Brien, T. P., Fennell, J. F., Claudepierre, S. G., Blake, J. B., Kilpua, E., & Hietala, H. (2015). The effects of geomagnetic storms on electrons in Earth's radiation belts. *Geophysical Research Letters*, *42*(21), 9176–9184. https://doi.org/10.1002/2015GL064747

Tuszewski, M., Cayton, T. E., Ingraham, J. C., & Kippen, R. M. (2004). Bremsstrahlung effects in energetic particle detectors. *Space Weather*, *2*(10), S10S01. https://doi.org/10.1029/2003SW000057

Wilkins, C., Angelopoulos, V., Runov, A., Artemyev, A., Zhang, X. J., Liu, J., & Tsai, E. (2023). Statistical characteristics of the electron isotropy boundary. *Journal of Geophysical Research (Space Physics)*, *128*(10), e2023JA031774. https://doi.org/10.1029/2023JA031774

Winant, A., Pierrard, V., & Botek, E. (2023). Comparison of radiation belt electron fluxes simultaneously measured with PROBA-V/EPT and RBSP/MagEIS instruments. *Annales Geophysicae*, *41*(2), 313–325. https://doi.org/10.5194/angeo-41-313-2023

Zhang, X.-J., Angelopoulos, V., Artemyev, A., Mourenas, D., Agapitov, O., Tsai, E., & Wilkins, C. (2023). Temporal scales of electron precipitation driven by whistler-mode waves. *Journal of Geophysical Research (Space Physics)*, *128*(1), e2022JA031087. https://doi.org/10.1029/2022JA031087

Zhao, H., Friedel, R. H. W., Chen, Y., Reeves, G. D., Baker, D. N., Li, X., et al. (2018). An empirical model of radiation belt electron pitch angle distributions based on van allen Probes measurements. *Journal of Geophysical Research (Space Physics)*, *123*(5), 3493–3511. https://doi.org/10.1029/2018JA025277